Design and Control of Wireless Hybrid Stepper Motor System

Songtao Li, *Graduate Student Member, IEEE*, K. T. Chau, *Fellow, IEEE*, Wei Liu, *Member, IEEE*,
Chunhua Liu, *Senior Member, IEEE*, and Chi-Kwan Lee, *Senior Member, IEEE*

***Abstract*—This article proposes and implements a wireless hybrid stepper motor (HSM) system, which offers high controllability of speed, direction, and position without physical contact and electrical connection between the power source and the motor. By transmitting electrical pulses to each motor winding in different frequencies, duty ratios, and sequences, the speed can be regulated to expected values, and the rotation angle of each step and direction can be controlled without any sensors or controllers at the secondary side. Two orthogonal bipolar coils and double-frequency resonant networks are adopted to provide four decoupled current channels to control the four self-drive switches independently at the secondary side. Thus, various operating modes can be realized for different working requirements. To equalize the power output at all phases, pulse frequency modulation is adopted to maintain robust zero-voltage switching. The motor can carry a 1.5-N·m load at the speed of 430 rpm and provides speed and position control capability. The theoretical analysis, computer simulations, and hardware experimentations are given to verify the feasibility of the proposed wireless HSM system.**

***Index Terms*—Double-frequency compensation network, frequency selection, pulse frequency modulation (PFM), wireless hybrid stepper motor (HSM), wireless power transfer (WPT).**

I. INTRODUCTION

Wireless power transfer (WPT) has been identified as one of the most epoch-making technologies in recent years. Based on the magnetic resonance coupling, the electromagnetic field delivers energy wirelessly without messy cables, thus bringing numerous advantages, such as high flexibility, safety, and mobility [1], [2]. Besides, the contactless power transfer allows the equipment to work in a sealed enclosure, which improves its robustness against watery and harsh environments [3]. After years of research and development, the WPT has been gradually commercialized in wireless charging for consumer electronics [4] and electric vehicles (EVs) [5], [6]. Also, it has shown great potential in other applications, such as wireless motoring [7], wireless energy encryption [8], and wireless sensor networks [9].

In recent years, wireless motors have drawn the attention of researchers. For traditional wired motors, when exposed to outdoor environments, the cables are fragile to bending and environmental impacts, which may cause disconnection [10]. By incorporating WPT in the motor system, the sparking hazards and messy wires can be eliminated, thus improving performance and convenience in various special applications, such as EVs, robotics, underground piping networks, and industrial manufacturing [11].

The concept of the wireless powered motor was first revealed by Sato et al. [7] to get rid of the cable abrasion in EVs, where a wireless in-wheel motor is powered by the WPT and controlled by an extra controller at the secondary side. This double-controller structure brings huge complexity and increases the maintenance needs. To solve this problem, several primary-controlled wireless motors have been proposed. A wireless permanent magnet (PM) dc motor was studied, where the motor speed can be regulated by adjusting the WPT output [12]. However, the carbon brushes and commutators are fragile and high cost. Another scheme of wireless switched reluctance motor was proposed, where three receivers are adopted to energize three separate windings [13]. The rotor position must be detected for commutation, and thus, the position sensor and communication module are essential, which makes the system bulky. Recently, a wireless ultrasonic motor was proposed, where the high-frequency current is injected into the motor directly and the motor-side circuit can be greatly simplified [14]. However, the accurate speed is still unknown to the controller without a speed sensor. For wireless motors that need bidirectional current in the winding, primary-controlled switches are used to change the current direction. Similar designs have emerged in wireless shaded pole induction motors [15] and wireless single-phase induction motors [16].

The performance of the wireless motors highly depends on the control methods. Unlike wired motors or double-controller wireless motors, the feedback control of the primary-controlled wireless motors is more challenging since an independent channel is needed for wireless data transmission. Bluetooth

Manuscript received 1 November 2023; revised 25 February 2024; accepted 12 April 2024. Date of publication 22 April 2024; date of current version 20 June 2024. This work was supported by the Hong Kong Research Grants Council, Hong Kong Special Administrative Region, China, under Grant T23-701/20-R, Grant 17206222, and Grant 17210621. Recommended for publication by Associate Editor L. Iyer. *(Corresponding author: K. T. Chau.)*

Songtao Li is with the Department of Electrical and Electronic Engineering, The University of Hong Kong, Hong Kong (e-mail: stli@eee.hku.hk).

K. T. Chau and Wei Liu are with the Research Centre for Electric Vehicles, The Hong Kong Polytechnic University, Hong Kong, and also with the Department of Electrical and Electronic Engineering, The Hong Kong Polytechnic University, Hong Kong (e-mail: k.t.chau@polyu.edu.hk; wei.liu@polyu.edu.hk).

Chunhua Liu is with the School of Energy and Environment, City University of Hong Kong, Hong Kong (e-mail: chunliu@cityu.edu.hk).

Chi-Kwan Lee is with the School of Electrical and Data Engineering, University of Technology Sydney, Sydney, NSW 2007, Australia (e-mail: CHIKWAN.LEE@uts.edu.au).

Color versions of one or more figures in this article are available at https://doi.org/10.1109/TPEL.2024.3392376.

Digital Object Identifier 10.1109/TPEL.2024.3392376

modules [13] and wireless resolvers [17] have been utilized for commutation control of wireless switched reluctance motors. However, the connection interval of Bluetooth breaks the phase synchronization at high speed, and the interference between the power and signal transfer channels reduces the robustness of the system. For most of the previous studies, open-loop control is still the mainstream method in which the speed and position control are inaccurate.

The controllability of the motor current and voltage is another key issue, which greatly affects the motor speed and maximum load. For multifrequency wireless motors, power equalization among phases is also essential. Generally, the output control methods of WPT can be classified into pulse width modulation (PWM), pulse density modulation (PDM), and pulse frequency modulation (PFM). The PWM is widely used to offer different outputs with variable duty ratios. Although it takes key merits of simple and high control precision, it suffers from high-frequency hard-switching loss during power regulation unless using a complicated zero-voltage switching (ZVS) control [18]. The PDM can maintain the ZVS to keep a high efficiency with variable output, while it brings slightly larger output fluctuations, and hence, the torque ripple of wireless motors increases [19]. Compared with the above methods, the PFM regulates the WPT output by modulating pulses between two switching frequencies, hence achieving the ZVS and generating a smooth output, which makes it suitable for wireless motors [20].

To provide the speed and position control capability using the primary-controlled wireless motor scheme, a stepper motor has unique advantages over other types of motors. Stepper motors are driven by electrical pulses that can determine the rotor position, direction, and speed [21]. The position is proportional to the number of pulses, and thus can provide the accurate speed and position control without feedback, which greatly simplifies the system structure and control complexity. A wireless individual-drive system for variable reluctance (VR) stepper motor was already proposed in [22] to make use of this advantage. The hybrid stepper motor (HSM) is a combination of VR stepper motor and PM stepper motor, which has high torque output and high angular resolution, which is widely accepted in practical applications.

In this article, a wireless HSM is newly proposed and implemented, which provides speed and position control capabilities without using any sensors or motor controllers at the secondary side. To reduce the number of switches, a unipolar stepper motor is adopted. Each switch retrieves the control signal through a self-drive circuit unit connected to decoupled current channels. Therefore, various operating modes can be realized. For the power equalization and output adjustment, the PFM strategy is integrated to achieve these targets while ensuring the ZVS. The proposed wireless HSM system can be used in robotic applications and industrial manufacturing facilities, where the position control is necessary. The elimination of wires brings convenience to the modular design, which allows the equipment to complete more functions by replacing some parts.

The rest of this article is organized as follows. Section II will introduce the system configuration, the operating principle of different operating modes, and the PFM-based power equalization. Section III will discuss the design of the double-frequency resonant networks on both sides. Also, the design and simulations of the decoupled couplers will be presented. Moreover, a generalized design method of the proposed system will be given. In Section IV, an experimental prototype will be constructed to verify the feasibility of the proposed wireless HSM system. The performance under different operating modes will also be compared. Finally, Section V concludes this article.

II. System Configuration and Control Principle

A. System Configuration

The topology of the proposed wireless HSM system is shown in Fig. 1, which comprises two silicon carbide (SiC) half-bridge inverters, two pairs of double-frequency resonant compensated transmitters and receivers, two rectifiers, four self-drive SiC switch units, and a unipolar HSM. Each motor phase is connected to one pair of transmitter and receiver, forming two decoupled power channels. According to the structure of the motor, currents are injected into wire leads $A+$, $A-$, $B+$, and $B-$ to provide magnetic fields in two directions without the need to change the direction of output currents. To provide the current paths and avoid the uncontrollable induced currents in idled windings, a self-drive switch is connected to each wire lead directly. Following the previous design reported in [15], the self-drive switches can extract control signals from the voltages on specific capacitors, and the switch control can be completed by using the different transmitting frequencies. Therefore, the power is generated in two frequencies in one channel to achieve the independent control on both switches. In this system, four operating frequencies f_i ($i = 1, 2, 3, 4$) are used in total, and the high-order compensation circuits provide multiple resonant frequencies for higher efficiency and good selectivity. In the proposed design, $f_1 = 150$ kHz, $f_2 = 300$ kHz, $f_3 = 125$ kHz, and $f_4 = 250$ kHz.

In Fig. 1, L_{tpa}, C_{tpa}, C_{ta}, L_{ta}, L_{tpb}, C_{tpb}, C_{tb}, and L_{tb} with subscripts a and b denote the inductances and capacitances of parallel-connected LC tanks, series-connected capacitances, and transmitter coil inductances of the primary-side compensation circuits in channels A and B, respectively. M_a and M_b are the mutual inductances of the coils in two channels. L_{ra}, C_{ra}, L_{rpa1}, C_{rpa1}, L_{rpa2}, C_{rpa2}, C_{ap}, and C_{an} constitute the channel A compensation circuit resonants at f_1 and f_2, wherein L_{rpa1}, C_{rpa1}, L_{rpa2}, and C_{rpa2} form two band-stop filters with the center frequencies of f_2 and f_1, respectively. Therefore, the current under f_1 and f_2 will have different paths. The receiver circuit of channel B has a similar structure as that of channel A, with different subscripts of b. R_{ta}, R_{tb}, R_{ra}, and R_{rb} denote the internal resistances of transmitter and receiver coils. u_a, u_b, i_{ta}, i_{tb}, i_{rap}, i_{ran}, i_{rbp}, and i_{rbn} represent the input voltages, transmitter currents, and currents in decoupled channels. i_{ap}, i_{an}, i_{bp}, and i_{bn} are the phase currents of $A+$, $A-$, $B+$, and $B-$. S_{ap}, S_{an}, S_{bp}, and S_{bn} denote the self-drive switches connected to the motor.

In order to prevent the switches from unexpectedly turning on, voltages on capacitors C_{ap}, C_{an}, C_{bp}, and C_{bn} are extracted as

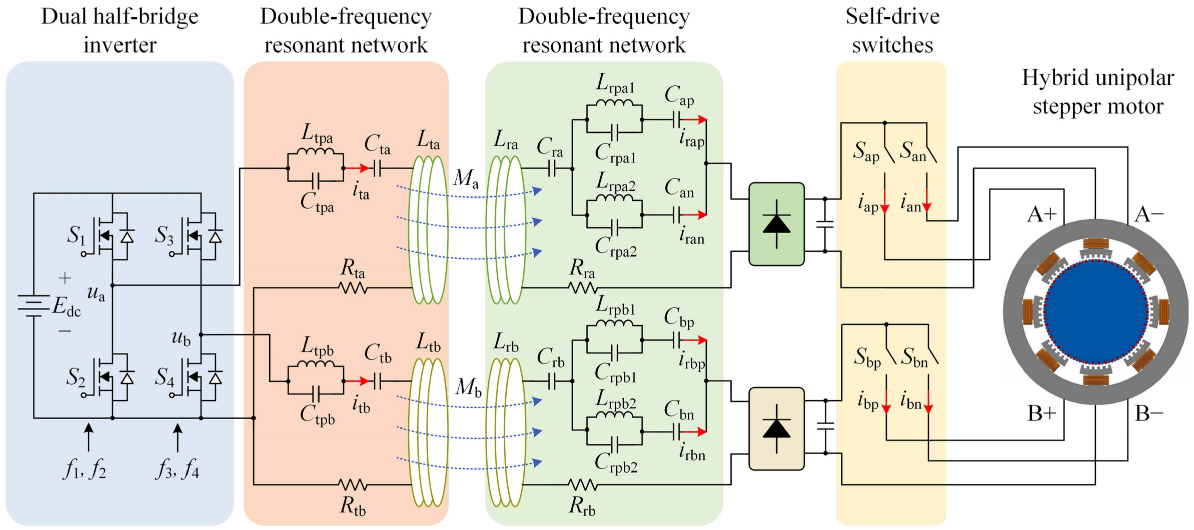

Fig. 1. System topology of the proposed wireless HSM system.

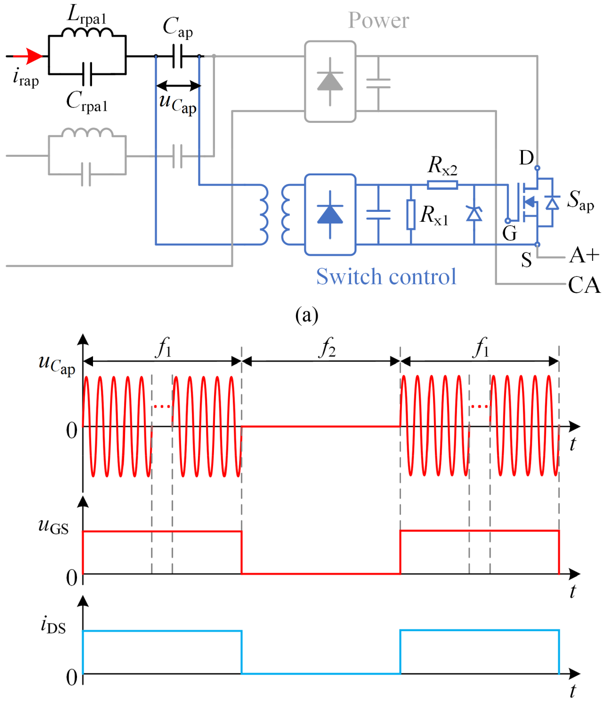

(a)

(b)

Fig. 2. Self-drive circuit of secondary-side switch S_{ap} and its working principle. (a) Self-drive circuit topology. (b) Working principle of switch on/off control.

control signals. Fig. 2(a) shows the structure of the self-drive circuit connecting to S_{ap}. The voltage u_{Cap} over C_{ap} is first isolated by a transformer, rectified, and then stabilized to generate a stable control signal on the switch. A Zener diode with a breakdown voltage of 18 V is connected between the gate and the source of SiC switch for protection. The working principle is shown in Fig. 2(b). Taking S_{ap} as an example, when the transmitting frequency f equals f_1, u_{Cap} is enough to turn on S_{ap}, while u_{Cap} is greatly suppressed to turn off S_{ap} when $f = f_2$. S_{an}, S_{bp}, and S_{bn} have the same structure and working principle as S_{ap} does, thus providing independent control capability to all four secondary-side switches.

B. Operating Principle

The stepper motor is powered by electric pulses injected into each phase. The sequence and time of the pulses affect the direction, speed, and maximum output torque. In the proposed wireless HSM system, three basic operation modes of their wired counterparts are implemented: wave drive, full-step drive, and half-step drive. Thanks to the independent control of self-drive switches, the system can generate the same electric pulses of traditional wired stepper motors with the proposed WPT system; therefore, no modifications have to be made to the motor itself. Fig. 3 shows the operating principle of each mode when rotating counterclockwise. The stator windings are energized in a looped sequence for a stable rotating magnetic field. T_c is defined as the control period to represent the time containing a full sequence loop.

In the wave drive, only one phase is energized at any given time. In the wired unipolar HSM, the current is injected into the stator winding in the sequence of $A+ \rightarrow B+ \rightarrow A- \rightarrow B-$. In the proposed system, as shown in Fig. 3(a), the primary-side inverters generate power in variable frequencies following the sequence of $f_1 \rightarrow f_3 \rightarrow f_2 \rightarrow f_4$, generating the same electrical pulses as the wired motors. The rotor rotates one step angle every pulse comes. The motor speed n can be expressed in rpm as follows:

$$n = \frac{2\theta_e}{3T_c} \tag{1}$$

where θ_e is the step angle of the motor. However, the maximum torque output of wave drive mode is limited due to the low utilization of windings. The wave drive mode is suitable for

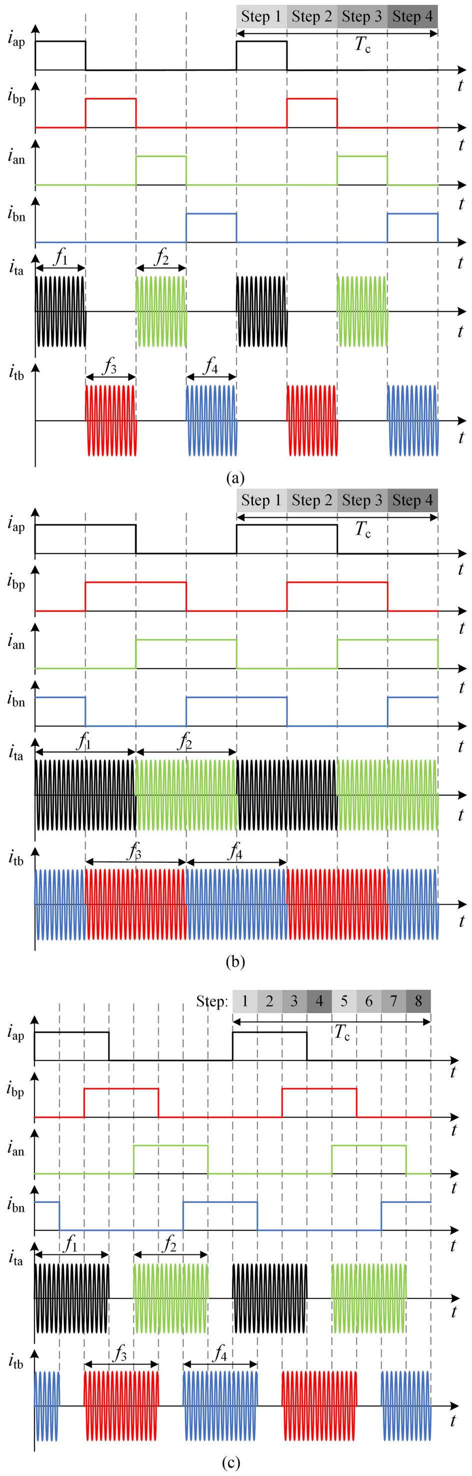

Fig. 3. Operating principles of the proposed wireless HSM system in different drive modes. (a) Wave drive mode. (b) Full-step drive mode. (c) Half-step drive mode.

applications where reduced power consumption is important and high torque is unnecessary, such as 3-D printers, disk drivers, and scanners.

The full-step drive provides higher torque output compared with wave drive mode. However, two phases are energized at the same time. Fig. 3(b) shows the ideal motor phase currents and transmitter currents in both power channels. In one control period, the currents are injected following the sequence of $A+B- \rightarrow A+B+ \rightarrow A-B+ \rightarrow A-B-$, while the frequencies of the transmitter current are $f_1f_4 \rightarrow f_1f_3 \rightarrow f_2f_3 \rightarrow f_2f_4$. The motor speed in full-step drive can also be derived as (1), and the rotation angle of each step is the same as wave drive. Due to high torque output, the full-step drive mode can be used in nearly all the suitable applications for stepper motors, especially robotics, computer numerical control (CNC) machines, textile machines, and applications where high torque is necessary.

The step angle of the motor is defined by the structure. To further increase the resolution of the angle, half-step drive and microstepping control have been presented to decrease the resolution to half of the step angle or even smaller. In the proposed system, the half-step drive mode is utilized for exemplification, and higher resolution can be readily achieved by using a similar principle. Half-step drive mode is a combination of wave drive and full-step drive that generates smoother stator current and higher angle resolution. As shown in Fig. 3(c), the number of excited phases alternates between 1 and 2. During one control period, the phases are energized in the sequence of $A+B- \rightarrow A+ \rightarrow A+B+ \rightarrow B+ \rightarrow A-B+ \rightarrow A- \rightarrow A-B- \rightarrow B-$. The switching frequency of the primary-side inverters is $f_1f_4 \rightarrow f_1 \rightarrow f_1f_3 \rightarrow f_3 \rightarrow f_2f_3 \rightarrow f_2 \rightarrow f_2f_4 \rightarrow f_4$. The rotation angle at each step is half of the step angle theoretically, leading to less torque ripple; the motor speed remains unchanged with the same control period and step angle. The high angular resolution brings a wide range of practical applications, especially for those who need accurate position via simple open-loop control, such as robotics, CNC machines, 3-D printers, and medical equipment.

All three operation modes can be simply realized by the proposed system, offering different angular resolutions. In all three operation modes, when rotating counterclockwise, the starting time of each transmitting frequency in a single control period is 0, $T_c/2$, $T_c/4$, and $3T_c/4$ for $f_1, f_2, f_3,$ and f_4, respectively. Furthermore, when operating in a specific mode, each electric pulse occupies the same portion in a control period. The duty ratio of electrical pulses is defined as δ_p to describe the pulse time compared with the control period, which can be calculated as follows:

$$\delta_p = \frac{t_p}{T_c} \tag{2}$$

where t_p is the time of each pulse. As shown in Fig. 3, δ_p is 1/4, 1/2, and 3/8 in wave drive mode, full-step drive mode, and half-step drive mode. When rotating clockwise, the electric pulses are generated following the reverse order of that in rotating counterclockwise. However, the starting time of each transmitting frequency in a single control period is 0, $T_c/2$, $3T_c/4$, and $T_c/4$ for $f_1, f_2, f_3,$ and f_4, respectively.

C. PFM-Based Power Equalization

In the proposed wireless HSM system, four operating frequencies are adopted for independent control of self-drive switches. As each half of the phase winding is energized by wireless power in different frequencies, the output current under different frequencies must be equalized to ensure the smooth operation

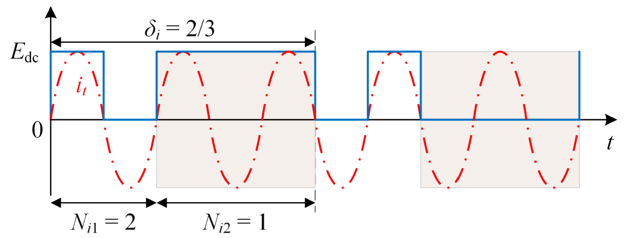

Fig. 4. Theoretical waveform of half-bridge inverter output voltage and current using PFM.

of the motor. Moreover, for the light-load condition, the motor current can be regulated below the rated value to reduce the heat loss.

In the proposed wireless HSM system, PFM is integrated to regulate the output current. The switching frequency of inverters is modulated in f_i and $f_i/3$ ($i = 1, 2, 3, 4$) alternately for lower output. The PFM duty ratio δ_i for f_i is defined as [20] follows:

$$\delta_i = \frac{N_{i1}}{N_{i1} + N_{i2}},\ (N_{i1}, N_{i2} \in N,\ i = 1, 2, 3, 4) \tag{3}$$

where N_{i1} and N_{i2} represent the minimum numbers of half-cycles in T_i and $3T_i$, respectively. The theoretical waveform of the half-bridge inverter outputs using PFM is shown in Fig. 4.

The Fourier expansion of the half-bridge inverter output voltage $u(t)$ using PFM can be derived as follows:

$$\begin{aligned} u(t) &= a_0 + \sum_{n=1}^{\infty} (a_{in} \cos 2\pi n f_i t + b_{in} \sin 2\pi n f_i t) \\ &= \frac{1}{N_{i1}T_i + 3N_{i2}T_i} \int_0^{N_{i1}T_i + 3N_{i2}T_i} v(t) dt \\ &\quad + \frac{2}{N_{i1}T + 3N_{i2}T} \left(\int_0^{N_{i1}T_i + 3N_{i2}T_i} v(t) \cos 2\pi n f_i t dt \right) \\ &\quad \cdot \cos 2\pi n f_i t \\ &\quad + \frac{2}{N_{i1}T_i + 3N_{i2}T_i} \left(\int_0^{N_{i1}T_i + 3N_{i2}T_i} v(t) \sin 2\pi n f_i t dt \right) \\ &\quad \cdot \sin 2\pi n f_i t \end{aligned} \tag{4}$$

where

$$v(t) = \frac{(-1)^{k-1} E_{dc} + E_{dc}}{2}, k \in (1, +\infty). \tag{5}$$

The amplitude of the fundamental component of the PFM-modulated voltage output for a half-bridge inverter can be calculated as

$$v_1(t) = \frac{2E_{dc}}{\pi} \frac{1}{3 - 2\delta_i}. \tag{6}$$

Since the output is mainly determined by the fundamental component of the inverter output, by setting a lower PFM duty ratio, the motor current injected into each motor input can be equalized according to the output under the highest transmitting frequency. In the proposed system, δ_2 is set to 1 and the other duty ratios are reduced to different values for equalized output.

Another unique advantage of PFM is the elimination of even-order harmonics at all output levels and reducing of switching frequency. The parameters a_{in} and b_{in} in (4) maintain zero when n is even, while in PWM, the output voltage of a half-bridge inverter can be expressed as follows:

$$u_{\mathrm{PWM}}(t) = dE_{dc} + \frac{2E_{dc}}{\pi n} \sin(\pi n d) \cdot \cos(2\pi n f_i t) \tag{7}$$

which will contain the even-order harmonics when the duty ratio is $d<50\%$. The elimination of even-order harmonics brings great convenience to the decoupling design of the secondary-side circuit and the deviation between the transmitting frequencies can be reduced while maintaining high decoupling performance; thus, the frequency range of transmitting frequencies can be limited, and the input voltage level of the system can be reduced in the scenarios when large output current is needed.

III. DOUBLE-FREQUENCY HIGH-ORDER COMPENSATION DESIGN

The characteristics of the proposed WPT system highly depend on the structure of compensation circuits. In the previous research about wireless motors and multiload WPT systems, the high-frequency wireless power is transferred in different frequencies to energize the selected load or motor phase only. A switched capacitor array [13] and an *LCC* compensation [23] can provide multiple resonant frequencies. The switched capacitor can fully compensate for all the operating frequencies flexibly. However, it brings huge voltage stress on the switches. The *LCC* compensation provides three resonant frequencies, while only one frequency is fixed against the variation of the coupling coefficient. To solve these problems, some higher order compensation networks are designed, such as *C-LCC* [15] and *LCLC* networks [24], which have two stable resonant frequencies. A multiple-frequency resonating compensation network is proposed for multiple pick-up systems [25], which provides two resonant frequencies in the same order as *LCC* compensation. To reduce the number of components in the proposed system, the compensation network at the primary side is designed following the same method in [25]. To control the self-drive switches independently, the compensation network at the secondary side is designed to offer separate channels for currents at each frequency. Totally four current channels are needed for the self-drive switches. In the proposed design, two current paths are provided in each channel, and the interference between channel *A* and channel *B* is eliminated by the decoupled magnetic couplers. Since the circuits in both channels have the same structure, the following circuit analysis will use channel *A* for exemplification, and the equivalent circuit is shown in Fig. 5.

A. Primary-Side Double-Frequency Network

In Fig. 5, the double-frequency compensation network is composed of a series-connected *LC* (L_{ta}, C_{ta}), and a parallel-connected *LC* (L_{tpa}, C_{tpa}). The inductances of the transmitter coil L_{ta} and the resonant frequencies f_1 and f_2 ($f_1<f_2$) are predefined. For simplicity, the ratio of the inductances, capacitances,

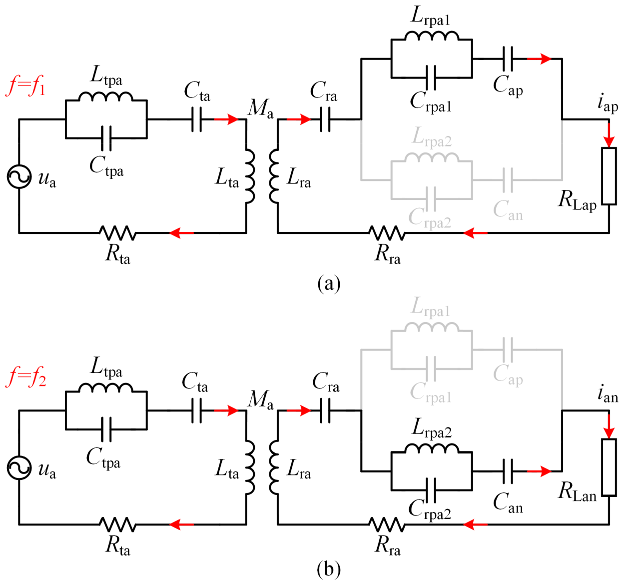

Fig. 5. Equivalent circuit of compensation network in channel *A* under f_1 and f_2. (a) f_1. (b) f_2.

and frequencies can be defined as $\alpha_L = L_{ta}/L_{tpa}$, $\alpha_C = C_{ta}/C_{tpa}$, and $\alpha_f = f_2/f_1$.

When the circuit works in the resonant frequencies, it yields

$$\begin{aligned}&\mathrm{Im}\left(Z_{\mathrm{ta}}\right)\\&=\mathrm{Im}\left(j\omega_i L_{ta}+\frac{1}{j\omega_i C_{ta}}+\frac{j\omega_i L_{tpa}}{1-\omega_i^2 L_{tpa}C_{tpa}}+Z_{reqa}+R_{ta}\right)\\&=\frac{\omega_i^2(L_{ta}C_{ta}+L_{tpa}C_{tpa}+C_{ta}L_{tpa})-\omega_i^4 L_{ta}L_{tpa}C_{ta}C_{tpa}-1}{\omega_i C_{ta}\left(1-\omega_i^2 L_{tpa}C_{tpa}\right)}\end{aligned} \tag{8}$$

where the imaginary part of the input impedance is zero, and $\omega_i = \omega_1$ or ω_2. To determine the value of capacitances in the compensation circuit, the resonant frequency of the series-connected *LC* and parallel-connected *LC* can be defined as

$$\begin{aligned}&f_{L_{ta}C_{ta}}\\&=\frac{f_1}{\sqrt{\frac{1}{2}+\frac{\alpha_C}{2}\left(1+\alpha_L-\sqrt{\left(\frac{\alpha_L\alpha_C-1}{\alpha_C}\right)^2+2\left(\frac{\alpha_L\alpha_C+1}{\alpha_C}\right)+1}\right)}}\end{aligned} \tag{9}$$

$$\begin{aligned}&f_{L_{tpa}C_{tpa}}\\&=\frac{f_2}{\sqrt{\frac{1}{2}+\frac{1}{2\alpha_L}\left(1+\frac{1}{\alpha_C}+\sqrt{\left(\frac{\alpha_L\alpha_C-1}{\alpha_C}\right)^2+2\left(\frac{\alpha_L\alpha_C+1}{r_C}\right)+1}\right)}}.\end{aligned} \tag{10}$$

Assuming f_1, f_2, L_{ta}, and L_{tpa} are predefined, the α_C can be calculated by dividing (10) by (9) as given by

$$\alpha_C=\frac{\begin{array}{c}\left(\alpha_f^4+1\right)\alpha_L-2\alpha_f^2\\+\sqrt{\left(\alpha_f^4-1\right)^2\alpha_L^2-4\alpha_f^2\left(\alpha_f^4+2\alpha_f^2+1\right)\alpha_L}\end{array}}{2\left(\alpha_f^2\alpha_L^2+2\alpha_f^2\alpha_L+\alpha_f^2\right)} \tag{11}$$

and α_L needs to satisfy (12) so as to ensure a real solution

$$\alpha_L>\frac{4\alpha_f^2\left(\alpha_f^4+2\alpha_f^2+1\right)}{\left(\alpha_f^4-1\right)^2}. \tag{12}$$

Therefore, the capacitances can be calculated as

$$\begin{cases}C_{ta}=\frac{1}{\left(2\pi f_{L_{ta}C_{ta}}\right)^2 L_{ta}}\\C_{tpa}=\frac{C_{ta}}{\alpha_C}.\end{cases} \tag{13}$$

According to the above analysis, for a fixed L_{ta}, the value of L_{tpa} can be chosen in a wide range, while the resonant frequencies remain unchanged. Due to the parallel *LC* structure, the currents flowing through L_{tpa} and C_{tpa} satisfy the relationship in (14) and can be expressed by the transmitter current i_{ta} in (15) and (16) as given by

$$i_{C_{tpa}}=-\omega_i{}^2 L_{tpa}C_{tpa}i_{L_{tpa}} \tag{14}$$

$$i_{L_{tpa}}=\frac{\omega_{L_{tpa}C_{tpa}}^2 i_{ta}}{\left(\omega_{L_{tpa}C_{tpa}}^2-\omega^2\right)} \tag{15}$$

$$i_{C_{tpa}}=-\frac{\omega^2 i_{ta}}{\left(\omega_{L_{tpa}C_{tpa}}^2-\omega^2\right)} \tag{16}$$

which proves that the currents in parallel-connected *LC* have a phase delay of 180°. For a constant current i_{ta}, the amplitudes of currents i_{Ltpa} and i_{Ctpa} vary with the inductance of L_{tpa} and the predefined resonant frequencies, which greatly affects the efficiency and voltage stress. According to (15) and (16), i_{Ltpa} and i_{Ctpa} have lower values when f_1 and f_2 have larger intervals. In the proposed design, the resonant frequencies are chosen as $f_1 = 150$ kHz, $f_2 = 300$ kHz, $f_3 = 125$ kHz, and $f_4 = 250$ kHz.

Within the range of possible values of *LC* components, the internal resistances of L_{tpa} and C_{tpa} are close, which are assumed to be equal. Thus, the power loss on L_{tpa} and C_{tpa} during one control period of full-step drive mode can be evaluated by

$$\begin{aligned}&i_{L_{tpa\_\omega 1}}^2+i_{C_{tpa\_\omega 1}}^2+i_{L_{tpa\_\omega 2}}^2+i_{C_{tpa\_\omega 2}}^2\\&=i_{ta}^2\left[\frac{\omega_{L_{tpa}C_{tpa}}^4+\omega_1^4}{\left(\omega_{L_{tpa}C_{tpa}}^2-\omega_1^2\right)^2}+\frac{\omega_{L_{tpa}C_{tpa}}^4+\omega_2^4}{\left(\omega_{L_{tpa}C_{tpa}}^2-\omega_2^2\right)^2}\right]\end{aligned} \tag{17}$$

where ω is the angular frequency.

Fig. 6 shows the relationship between the inductance of L_{tpa} and the variation trend of current and power loss on a parallel *LC* tank. When the L_{tpa} is increasing, the currents at f_2 decrease, while they increase at f_1. The power loss on the

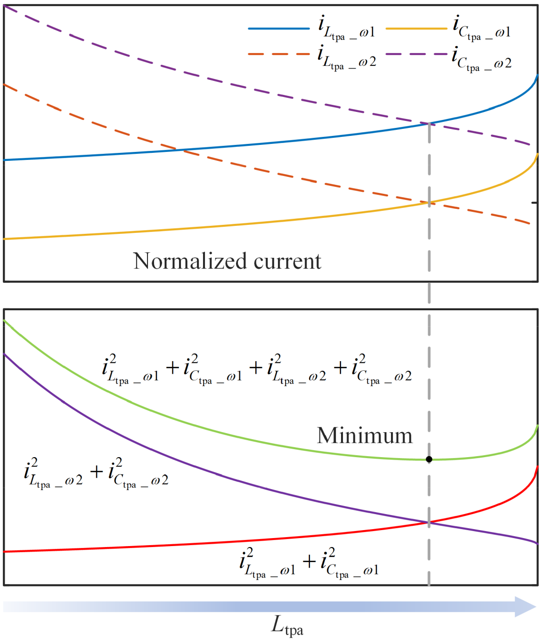

Fig. 6. Normalized current and power loss of parallel-connected *LC* tank against variable L_{tpa}.

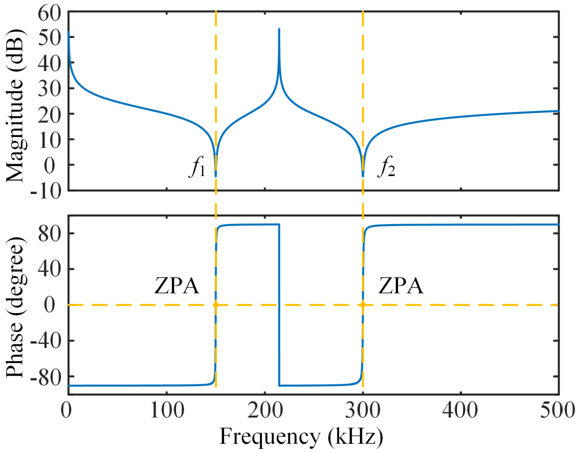

Fig. 7. Impedance characteristics of primary-side double-frequency compensation network.

parallel-connected *LC* tank reaches its minimum value when the power loss on f_1 and f_2 is equal, and the current amplitude is relatively low. The impedance characteristic of the compensation network is shown in Fig. 7. The circuit resonants at f_1 and f_2 and achieves zero-phase angle (ZPA) at each resonant frequency.

B. Secondary-Side Network With Frequency Selection

In Fig. 5, the secondary-side compensation network comprises two *LC* branches (L_{rpa1}, C_{rpa1}, C_{ap}; L_{rpa2}, C_{rpa2}, C_{an}). In each branch, a parallel-connected *LC* tank is used as a band-stop filter to provide separate current channels at each frequency, and thus, the parameters should be tuned as

$$\begin{cases}\omega_1=\dfrac{1}{2\pi\sqrt{L_{rpa2}C_{rpa2}}}\\ \omega_2=\dfrac{1}{2\pi\sqrt{L_{rpa1}C_{rpa1}}}.\end{cases}\tag{18}$$

Capacitors C_{ap} and C_{an} are connected to the band-stop filters in series to generate the control signals (u_{Cap}, u_{Can}) for self-drive circuits. The amplitudes are mainly affected by currents (i_{rap}, i_{ran}) and capacitances (C_{ap}, C_{an}) as given by

$$\begin{cases}u_{C_{ap}}=\dfrac{i_{rap}}{j\omega C_{ap}}\\ u_{C_{an}}=\dfrac{i_{ran}}{j\omega C_{an}}.\end{cases}\tag{19}$$

Generally, the gate–source voltage of MOSFET is set in the range from 7 to 20 V to keep a relatively low conduction loss while turning on and should be kept below 2 V to keep a stable turning off. The capacitances of C_{ap} and C_{an} are chosen to provide the control signal that falls in the desired range of gate–source voltage for switching on MOSFET. For full compensation, a capacitor C_{ra} is connected to both *LC* branches. The capacitance is selected to balance the voltage stress on both band-stop filters at f_1 and f_2, which can be derived as

$$C_{ra}=\frac{\omega_2-\omega_1}{\omega_1\omega_2L_r\left(\omega_1-\omega_2\right)+\frac{\omega_1}{C_{an}}-\frac{\omega_2}{C_{ap}}}.\tag{20}$$

Therefore, the parameters of the band-stop filters can be calculated by (18) and (21) as given by

$$\begin{cases}L_{rpa1}=\left(\frac{C_{ra}+C_{ap}}{\omega_1^2C_{ra}C_{ap}}-L_{ra}\right)\left(1-\frac{\omega_1^2}{\omega_2^2}\right)\\ L_{rpa2}=\left(\frac{C_{ra}+C_{an}}{\omega_1^2C_{ra}C_{an}}-L_{ra}\right)\left(1-\frac{\omega_2^2}{\omega_1^2}\right).\end{cases}\tag{21}$$

The input impedance of the secondary-side compensation network can be calculated as

$$Z_{ra}=j\omega L_{ra}+\frac{1}{j\omega C_{ra}}+\frac{Z_{ap}Z_{an}}{Z_{ap}+Z_{an}}+R_{Lme}+R_{ra}\tag{22}$$

where

$$\begin{cases}Z_{ap}=\frac{1}{j\omega C_{ap}}+\frac{j\omega L_{rpa1}}{1-\omega^2L_{rpa1}C_{rpa1}}\\ Z_{an}=\frac{1}{j\omega C_{an}}+\frac{j\omega L_{rpa2}}{1-\omega^2L_{rpa2}C_{rpa2}}.\end{cases}\tag{23}$$

R_{Lme} is the equivalent load before rectification, and R_{ra} represents the internal resistance of the receiver coil. The impedance characteristics of Z_{ap} and Z_{an} are shown in Fig. 8. However, Z_{ap} and Z_{an} have high impedance at f_2 and f_1, respectively. Fig. 9 shows the impedance characteristics of the magnitude and phase of the secondary circuit. The resonant frequencies are independent of load variations, and the robust ZPA operation can be achieved.

C. Decoupled Double-Phase WPT Coupler

The proposed wireless HSM has four current outputs for the two sets of unipolar windings. In previous studies, for the wireless motors with multiple windings, both one-to-many topology [13] and decoupled magnetic couplers [17] were reported. To eliminate the interference of the one-to-many structure, multiple receivers need to be placed at a large gap to reduce the mutual

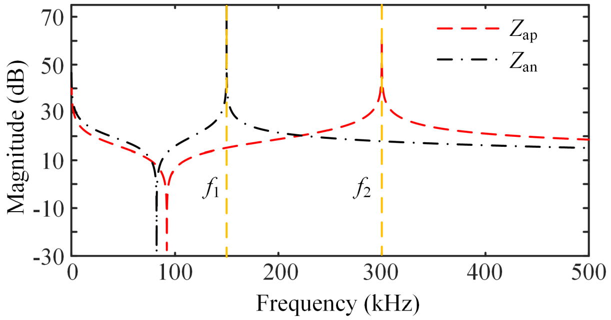

Fig. 8. Impedance characteristics of the current channels in channel A.

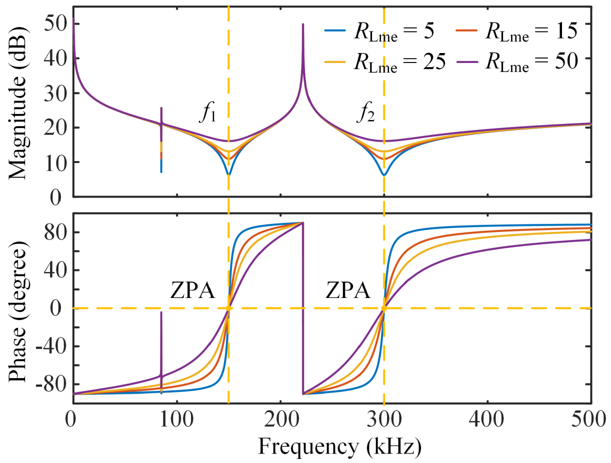

Fig. 9. Impedance characteristics of secondary-side double-frequency compensation network.

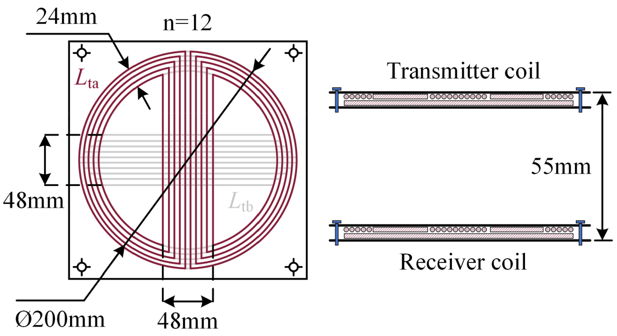

Fig. 10. Geometric dimension of decoupled double-phase WPT coils.

inductance between unrelated coils, which occupy a large space. By placing bipolar coils orthogonally, the multiple transmitter or receiver coils can be coaxially attached tightly, and the size of the magnetic coupler can be greatly reduced. The geometric dimensions of the magnetic coupler used in the proposed system are shown in Fig. 10.

A finite-element analysis (FEA) model is built according to the geometric parameters in Fig. 10 to estimate the magnetic field distributions. Fig. 11 shows the current densities in the coils and the magnetic flux densities along the middle parallel plane between two sets of coils at f_3 and f_4 when the output current is kept at 4 A. When energizing channel B only, the current in channel A is nearly zero, which proves that the two channels are decoupled by the orthogonal bipolar coils.

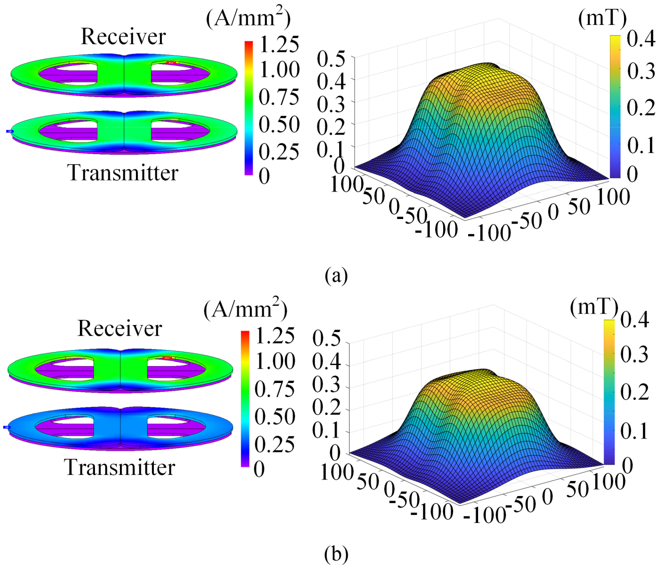

(a)

(b)

Fig. 11. FEA results of current densities and magnetic flux densities along the middle parallel plane between transmitter and receiver coils in channel B. (a) At operating frequency f_3. (b) At operating frequency f_4.

D. System Design Procedure

The flowchart of the design procedure of the proposed wireless HSM system is depicted in Fig. 12. In the design of the primary-side double-frequency compensation network, the parameters are only related to the transmitting frequencies, which are not related to the motor parameters. In the design of the secondary-side compensation network, the amplitudes of u_{Cap}, u_{Can}, u_{Cbp}, and u_{Cbn} are designed to fall in the desired range of gate–source voltage for switching on MOSFET at motor rated current; therefore, the values of C_{ap}, C_{an}, C_{bp}, and C_{bn} are affected by the motor rated current. For an existing system, an HSM with different parameters can also be incorporated, as long as the generated control signals are high enough to turn on the MOSFET. To ensure safe operation, the motor current should not far exceed the rated current adopted in the design procedure since high-voltage falls on the self-drive circuit might cause damage.

IV. EXPERIMENTAL VERIFICATION

A. Prototype Experimentation and Verification

In order to verify the feasibility of the proposed wireless HSM system, a prototype was built for experimental demonstration, as shown in Fig. 13. The design parameters and specifications of the prototype are listed in Table I. The inverter and self-drive switches are all populated with SiC MOSFETs of C3M0065090, and the rectifier adopts power diodes of STPS8H100D. The

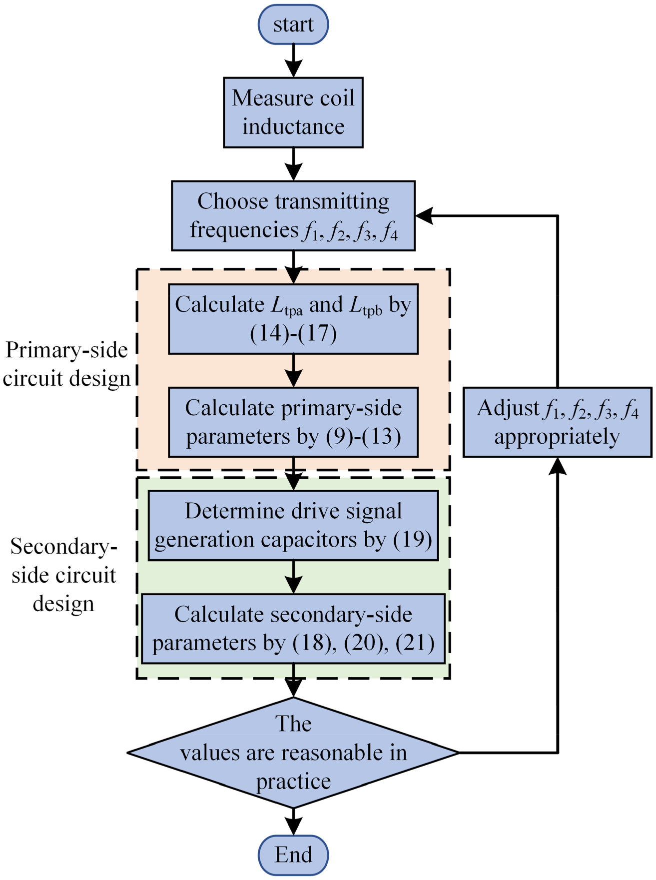

Fig. 12. Flowchart of the system design procedure.

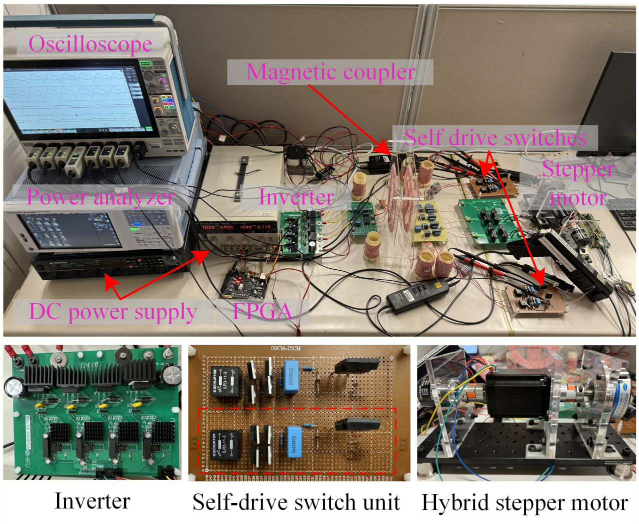

Inverter Self-drive switch unit Hybrid stepper motor

Fig. 13. Experimental setup of wireless HSM system.

TABLE I
DESIGN PARAMETERS AND SPECIFICATIONS OF THE PROTOTYPE

Parameters	Value/type
Transmitter	
Coil inductances (L_{ta}, L_{tb})	58.63, 58.56 μH
Coil internal resistances (R_{ta}, R_{tb})	0.15, 0.15 Ω
Transmitter compensation inductances (L_{tpa}, L_{tpb})	28.81, 27.7 μH
Transmitter compensation capacitances (C_{ta},C_{tb}, C_{tpa}, C_{tpb})	9.66, 14.23, 19.58, 28.01 nF
Receiver	
Coil inductances (L_{ra}, L_{rb})	55.67, 56.42 μH
Coil internal resistances (R_{ra}, R_{rb})	0.15, 0.15 Ω
Series connected capacitances (C_{ra}, C_{rb})	12.45, 18.43 nF
Band-stop filter capacitances (C_{rpa1}, C_{rpa2}, C_{rpb1}, C_{rpb2})	7.45, 14.84, 10.77, 21.66 nF
Band-stop filter inductances (L_{rpa1}, L_{rpa2}, L_{rpb1}, L_{rpb2})	37.11, 75.22, 37.69, 73.09 μH
Drive signal-generation capacitances (C_{ap}, C_{an}, C_{bp}, C_{bn})	70.79, 35.24, 84.77, 42.74 nF
Others	
Mutual inductances (M_a, M_b)	9.23, 9.92 μH
Resonant frequencies (f_1, f_2, f_3, f_4)	150.30, 301.20, 126.26, 252.53 kHz
Motor step angle	1.8 degree
Motor rated current	4 A
Transformer (ratio)	ILR3-11-3 (3:1)

WPT coils are wounded by 150×0.10 mm Litz wire according to the geometric dimensions in Fig. 10. The HSM has a rated current input of 4 A and a 1.8° step angle. A magnetic brake CD-HSY-20 with a maximum output torque of 2 N·m is loaded to the motor, and an incremental encoder E6B2-CWZ6C (2000 pulse/round) is mounted to the motor shaft for measuring rotor positions. The whole system is controlled by a field-programmable gate array (FPGA) controller (XC7Z020-2CLG400I) on the primary side. All the waveforms are recorded by an oscilloscope (Tektronix MSO58). All powers and efficiencies are measured by a precision power analyzer (YOKOGAWA WT5000).

First, four 2-Ω resistors are connected to imitate four unipolar windings for verifying the performance of PFM output regulation and the circuit. Fig. 14 shows the measured waveforms of the input voltages (u_a, u_b), input currents (i_{ta}, i_{tb}), switching control signals of the self-drive switches (u_{GSap}, u_{GSan}, u_{GSbp}, u_{GSbn}), and output currents (i_{ap}, i_{an}, i_{bp}, i_{bn}). The system operates in the full-step drive mode, and the commutation frequency of four channels is 150 Hz. The output current is tuned to approximately 4 A for all outputs, using different duty ratios of PFM ($\delta_1 = 4/7$, $\delta_2 = 1$, $\delta_3 = 1/2$, and $\delta_4 = 1$). As shown in Fig. 15, four self-drive switches turn on alternately as the targeted channel is activated, and the unrelated switches turn off, thanks to the frequency selection design of the secondary circuit. To avoid the shoot-through issues, sufficient dead time is inserted during the transition of frequencies. Fig. 14 also shows the zoom-in waveform under each operating frequency in the steady state. By using the PFM, the outputs can be equalized while the system works at different frequencies with nearly ZPA operation, and the inverter output voltage slightly leads the inverter output current to ensure ZVS operation.

For a practical wireless motor system, the stability against misalignment is also important; therefore, the maximum allowable misalignment is tested with the same load. Since the decoupled double-phase WPT coupler has the highest performance when placed orthogonally and coaxially, in this experiment, the receiver coil is moved from the aligned position along the *yb*-axis

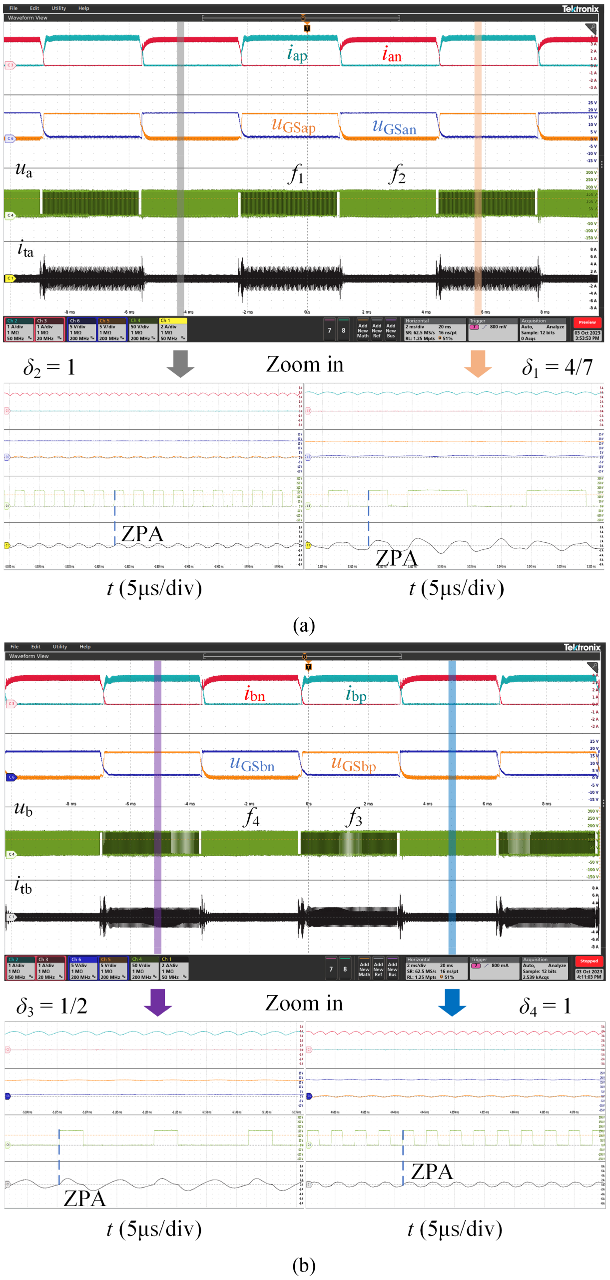

Fig. 14. Measured waveforms of the proposed wireless HSM system using unipolar-connected 2-Ω resistive load. (a) Measured waveform of channel *A*. (b) Measured waveform of channel *B*.

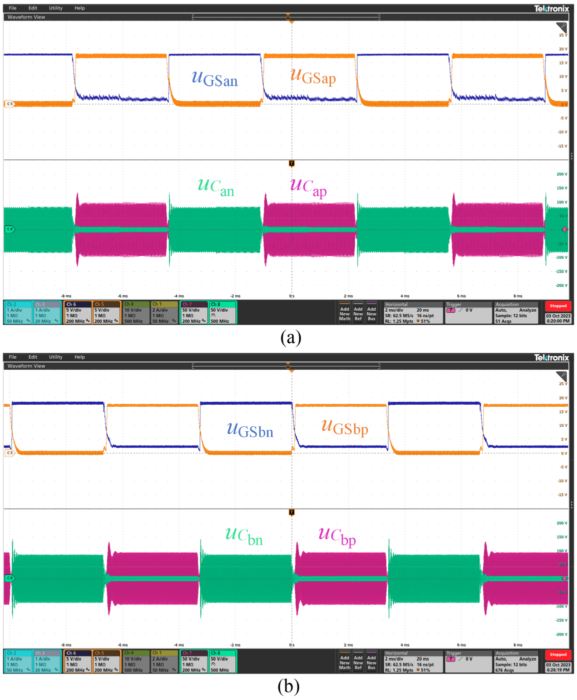

Fig. 15. Measured waveforms of frequency selection circuit and switching control signals. (a) Channel *A*. (b) Channel *B*.

of the channel *B* coupler, where all the 2-D misalignments can be decomposed along the *ya*-axis and *yb*-axis, as shown in Fig. 16(a). Fig. 16(b) shows the measured waveforms of the switching control signals of the self-drive switches (u_{GSap}, u_{GSan}, u_{GSbp}, u_{GSbn}) and output currents (i_{ap}, i_{an}, i_{bp}, i_{bn}) at the maximum misalignment of 38 mm. However, the unexpected turning on is caused by the interference from the current in another channel with close frequency. This fault first occurs on S_{an} and S_{bn} due to the lower capacitances of the corresponding signal-generation capacitors. Moreover, the output in channel *A* observed unequal amplitude caused by the misalignment along the *yb*-axis.

Second, the proposed system is loaded by an HSM. Three basic operation modes of wired stepper motors are realized. Fig. 17 shows the waveforms of motor phase currents and voltages of capacitors for drive signal generation. The control period is set as 5 ms to provide a motor speed of 240 rpm counterclockwise, and no-load is applied to the motor shaft. In the three operation modes, when the current is injected into a specific winding, only the targeted circuit branch is selected, which proves that each self-drive switch can be controlled independently and flexibly. Compared with the waveforms using pure resistive loads in Fig. 14, the phase currents increase slower due to the large inductance of motor windings. After the switch is turned off, the inverse induction current flowing through the other half of the unipolar winding is effectively suppressed by the positive current injected into it. This phenomenon does not affect the rotation of the motor since the electromagnetic force generated by the inverse current on the other half of the winding has the same direction.

Third, to test the dynamic performance of the proposed wireless HSM system, the speed control characteristic is tested against a constant load torque of 0.8 N·m in Fig. 18. The motor speed is controlled by setting the control period at the primary side. The motor starts at 120 rpm, speeds up to 360 rpm gradually with a step of 60 rpm, and then speeds down to 120 rpm with the same step. The motor rotates at each step for 4 s, and the dc input at the primary side is kept at 90 V.

The rotor position recorded by the incremental encoder is calculated by a DSP controller (TMS320F28335) every 10 ms. The result shows that the output speed is very close to the predefined value with a fast response, which proves the accurate speed and position control of the proposed wireless HSM

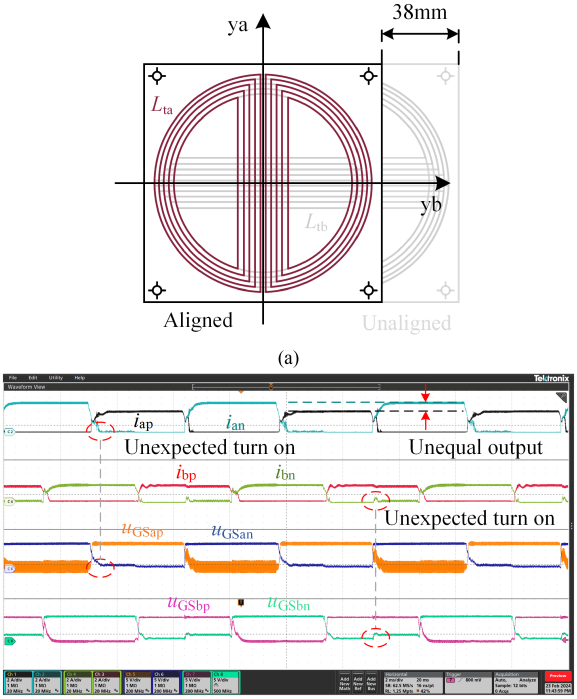

(a)

(b)

Fig. 16. Magnetic coupler position and measured waveforms of output current and switching control signals under maximum allowable misalignment of 38 mm. (a) Schematic of magnetic coupler position with misalignment of 38 mm. (b) Measured waveform of the output current and switching control signals.

system without sensors and feedback. Also, the waveforms of motor phase currents and voltages of capacitors for drive signal generation are recorded while the motor accelerates, as shown in Fig. 19. The motor speed is accelerated from 180 to 360 rpm directly with a constant load of 0.5 N·m.

To further evaluate the performance of position control, the rotor position is recorded by using the same method in the speed control. To provide sufficient resolution, the motor speed is set at 1 rpm. Fig. 20 shows the recorded rotor positions under full-step drive mode and half-step drive mode with a load torque of 0.8 N·m, wherein the motor rotates 360° counterclockwise. In Fig. 20(a), the recorded step angle is around 1.8° in full-step mode, which is the same as the step angle of the motor. Fig. 20(b) shows the recorded rotor position under half-step drive mode. The number of steps is doubled in the same period, thus providing higher resolution.

Furthermore, the maximum load against variable speed in three operation modes is evaluated in Fig. 21. The voltage of the dc power supply is kept constant at 120 V, and the input current of the magnetic brake is adjusted to provide different load torques. Similar to the wired stepper motors, among the three operation modes, the full-step drive mode provides the largest load capability at all speeds, while the maximum load torque offered by wave drive mode is only half of the full-step drive mode. Unlike the wired stepper motors, which achieve the largest load capability at low speeds, the maximum load capability of the proposed wireless HSM system shows a slight increase in higher speeds and it can be maintained with the speed increases. The reason is that the compensation circuit is

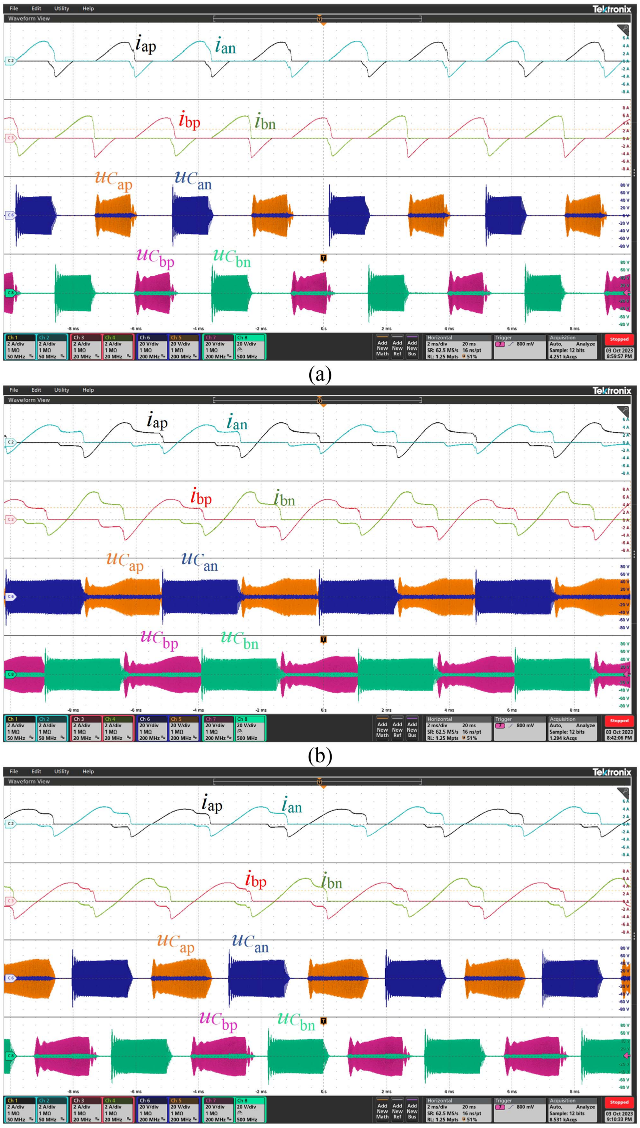

(a)

(b)

(c)

Fig. 17. Measured waveforms of the proposed wireless HSM in different operating modes under no-load conditions with a rotating speed of 240 rpm. (a) Wave drive mode. (b) Full-step drive mode. (c) Half-step drive mode.

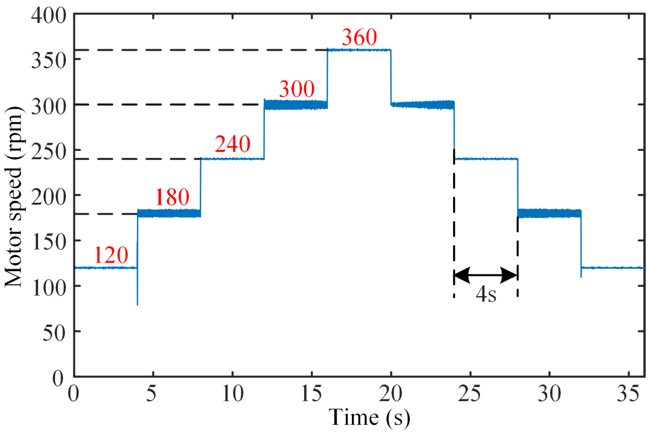

Fig. 18. Speed control characteristic of the proposed wireless HSM system under constant load of 0.8 N·m.

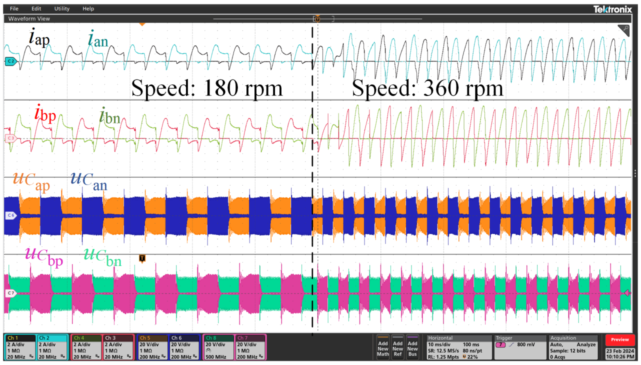

Fig. 19. Measured waveforms of the proposed wireless HSM when accelerating from 180 to 360 rpm under a constant load of 0.5 N·m.

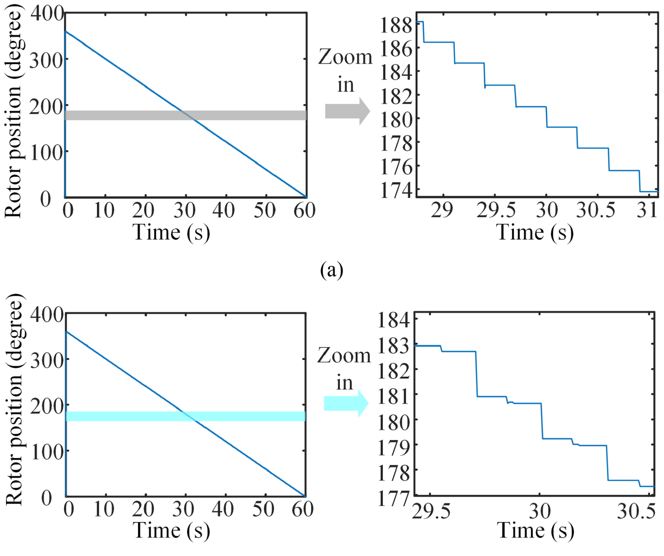

(a)

(b)

Fig. 20. Rotor position of the proposed wireless HSM system under 1 rpm speed and 0.8-N·m load torque. (a) Full-step drive mode. (b) Half-step drive mode.

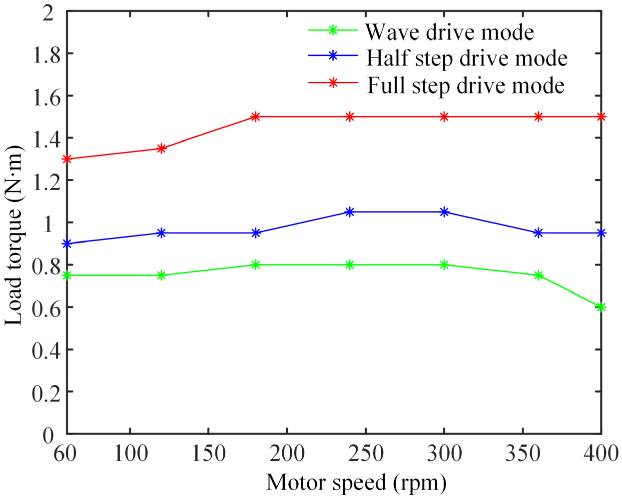

Fig. 21. Maximum load capability against variable speed in three operation modes.

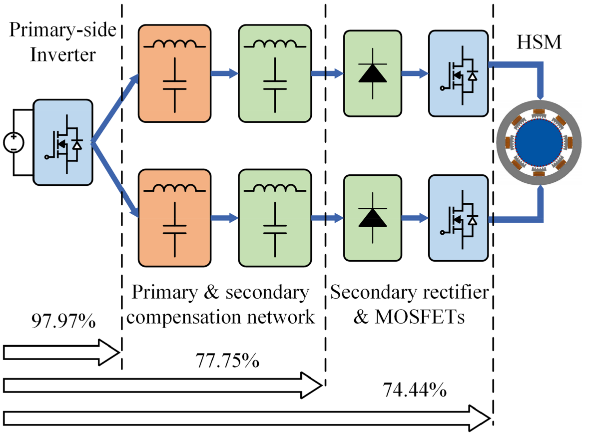

Fig. 22. Efficiencies at different stages of wireless HSM system under 90-V input, 300-rpm speed, and 1.1-N·m load.

series–series compensation when working under resonant frequencies, and the output current can be approximated as load independent [26].

According to Acarnley [27], the output torque of an HSM is determined by the input current and the number of energized phases. Therefore, with a constant power source at the primary side, the maximum output torque of the proposed wireless HSM system shows no dramatic decrease with increasing speed, and the full-step drive mode has the best load capability among the three operation modes. The motor can carry a 1.5-N·m load at 400 rpm speed.

Finally, the efficiency of the proposed wireless HSM system is tested. A specific condition with a 90-V dc input, 300-rpm speed, and 1.1-N·m load is analyzed as an example. Fig. 22 shows the efficiencies at different stages. The efficiency from the dc power source to the motor terminal is 74.44%. The compensation circuits on both the WPT sides consume most of the power loss before the motor terminal. The high-order compensation network of the proposed system provides double resonant frequencies and decoupled current paths; however, the number of *LC* components is large and the output current needed for driving the motor is also high, which reduces the overall efficiency. The loss on rectifiers and self-drive switches at the secondary side is reduced by using components with low conduction loss. The efficiency of the proposed system at a higher speed is also tested, which reaches 76.97% with a speed of 360 rpm and both the input and load are kept the same. To further test the efficiency under high-input high-load working conditions, the dc input is increased to 120 V and the speed is accelerated to 430 rpm, and the overall efficiency is 70.2%. When operating under high speeds or high-load conditions, the heat dissipation of the motor needs to be considered as the motor power increases, and the continuous working time should also be limited to prevent damage to the motor system.

B. Discussion and Recommendation

To highlight the novelty of the proposed wireless HSM system, a comprehensive comparison with the existing wireless motor systems is summarized in Table II. It can be observed

TABLE II
COMPARISON OF THE EXISTING WIRELESS MOTOR SYSTEMS AND PROPOSED WIRELESS HSM SYSTEM

Ref.	Controller	Communication modules	Bidirectional motion	Motor type	Transfer distance	System efficiency	Speed and position control
[11]	2 sides	0	Yes	PMSM	100 mm	92.51%	Yes
[12]	1 side	0	No	DC	1.5–3 m	89.1%	No
[13]	1 side	1	Yes	SRM	150 mm	72.8%	Yes
[14]	1 side	0	Yes	Ultrasonic	10 mm	87.2%	No
[15]	1 side	0	No	SPIM	20 mm	77%	No
[22]	1 side	1	Yes	VR	50 mm	87.5%	Yes
Proposed	1 side	0	Yes	HSM	55 mm	76.97%	Yes

that double controllers or communication modules are always needed for wireless motors that provide accurate speed and position control. The proposed wireless HSM system offers both speed and position control capabilities without any secondary-side controllers or communication units, and the bidirectional motion can also be simply realized in the control scheme, which improves reliability. Compared with the wireless VR stepper motor in [22], a higher angular resolution can be achieved by half-step drive mode even though the motor step angle is the same; also, a higher output torque can be achieved by full-step drive mode than the wave drive mode with the same motor, which provides a wide range of applications.

V. CONCLUSION

In this article, a wireless HSM system has been proposed and implemented. The proposed system eliminates the controllers, sensors, and communication modules at the secondary side by utilizing self-drive switches, thus improving the system's robustness. The compensation circuits at both primary and secondary sides are designed to provide double resonant frequencies, and the output of each phase is equalized using PFM, therefore realizing the ZVS operation on steady states. To realize multiple operating modes, all the self-drive switches can be switched on/off independently by providing separate channels for currents in different frequencies. The speed, direction, and position of the rotor can be controlled by changing the frequency of wireless power. Both computer simulations and prototype experimentations have been conducted to verify the feasibility of the proposed wireless HSM system. The experimental results show that the proposed system can carry a 1.5-N·m load under a speed of 430 rpm in full-step drive mode. The speed and rotor position can also be controlled without the need for sensors and feedback. This topology can be extended to other types of stepper motors, such as VR stepper motors and unipolar PM stepper motor, and also other motors with unipolar windings.

REFERENCES

[1] M. Song et al., "Wireless power transfer based on novel physical concepts," *Nature Electron.*, vol. 4, pp. 707–716, Oct. 2021.

[2] S. Li and C. C. Mi, "Wireless power transfer for electric vehicle applications," *IEEE J. Emerg. Sel. Topics Power Electron.*, vol. 3, no. 1, pp. 4–17, Mar. 2015.

[3] C. Liu, F. J. Lin, D. J. Thrimawithana, G. A. Covic, and M. Kesler, "Active impedance control for inductive charging of light-duty electric vehicles," *IEEE Trans. Power Electron.*, vol. 38, no. 11, pp. 13329–13340, Nov. 2023.

[4] Y. Zhang, S. Chen, X. Li, and Y. Tang, "Design methodology of free-positioning nonoverlapping wireless charging for consumer electronics based on antiparallel windings," *IEEE Trans. Ind. Electron.*, vol. 69, no. 1, pp. 825–834, Jan. 2022.

[5] X. Wang, L. He, J. Xu, C. K. Lee, and C. K. Tse, "Power-spilt-based wireless charging system with communication-free coordination control," *IEEE Trans. Power Electron.*, vol. 38, no. 2, pp. 2754–2767, Feb. 2023.

[6] S. Y. Jeong, J. H. Park, G. P. Hong, and C. T. Rim, "Autotuning control system by variation of self-inductance for dynamic wireless EV charging with small air gap," *IEEE Trans. Power Electron.*, vol. 34, no. 6, pp. 5165–5174, Jun. 2019.

[7] M. Sato, G. Yamamoto, D. Gunji, T. Imura, and H. Fujimoto, "Development of wireless in-wheel motor using magnetic resonance coupling," *IEEE Trans. Power Electron.*, vol. 31, no. 7, pp. 5270–5278, Jul. 2016.

[8] Z. Zhang, W. Ai, Z. Liang, and J. Wang, "Topology-reconfigurable capacitor matrix for encrypted dynamic wireless charging of electric vehicles," *IEEE Trans. Veh. Technol.*, vol. 67, no. 10, pp. 9284–9293, Oct. 2018.

[9] N. Aslam, K. Xia, and M. U. Hadi, "Optimal wireless charging inclusive of intellectual routing based on SARSA learning in renewable wireless sensor networks," *IEEE Sensors J.*, vol. 19, no. 18, pp. 8340–8351, Sep. 2019.

[10] Y. Chen, C. Gan, H. Shi, K. Ni, Z. Yang, and R. Qu, "Auxiliary circuit free maximum power efficiency tracking scheme for wireless motor system with source-load coupling," *IEEE Trans. Ind. Electron.*, vol. 70, no. 4, pp. 3414–3425, Apr. 2023.

[11] C. Li, Z. Wang, and Y. Xu, "A wireless-power-transfer-based three-phase PMSM drive system with matrix converter," *IEEE Trans. Ind. Electron.*, vol. 70, no. 3, pp. 2307–2317, Mar. 2023.

[12] W. Liu, K. T. Chau, H. Wang, and T. Yang, "Long-range wireless power drive using magnetic extender," *IEEE Trans. Transp. Electrific.*, vol. 9, no. 1, pp. 1897–1909, Mar. 2023.

[13] C. Jiang, K. T. Chau, C. Liu, and W. Han, "Design and analysis of wireless switched reluctance motor drives," *IEEE Trans. Ind. Electron.*, vol. 66, no. 1, pp. 245–254, Jan. 2019.

[14] Z. Xue, K. T. Chau, W. Liu, and Z. Hua, "Magnetic-free wireless self-direct drive motor system for biomedical applications with high-robustness," *IEEE Trans. Power Electron.*, vol. 39, no. 2, pp. 2882–2891, Feb. 2024.

[15] H. Wang, K. T. Chau, C. H. T. Lee, and C. Jiang, "Wireless shaded-pole induction motor with half-bridge inverter and dual-frequency resonant network," *IEEE Trans. Power Electron.*, vol. 36, no. 12, pp. 13536–13545, Dec. 2021.

[16] W. Liu, K. T. Chau, C. H. T. Lee, L. Cao, and W. Han, "Wireless power and drive transfer for piping network," *IEEE Trans. Ind. Electron.*, vol. 69, no. 3, pp. 2345–2356, Mar. 2022.

[17] H. Wang, K. T. Chau, C. H. T. Lee, and X. Tian, "Design and analysis of wireless resolver for wireless switched reluctance motors," *IEEE Trans. Ind. Electron.*, vol. 70, no. 3, pp. 2221–2230, Mar. 2023.

[18] Y. Jiang, L. Wang, Y. Wang, J. Liu, X. Li, and G. Ning, "Analysis, design, and implementation of accurate ZVS angle control for EV battery charging in wireless high-power transfer," *IEEE Trans. Ind. Electron.*, vol. 66, no. 5, pp. 4075–4085, May 2019.

[19] H. Li, J. Fang, S. Chen, K. Wang, and Y. Tang, "Pulse density modulation for maximum efficiency point tracking of wireless power transfer systems," *IEEE Trans. Power Electron.*, vol. 33, no. 6, pp. 5492–5501, Jun. 2018.

[20] W. Liu, K. T. Chau, C. H. T. Lee, W. Han, X. Tian, and W. H. Lam, "Full-range soft-switching pulse frequency modulated wireless power transfer," *IEEE Trans. Power Electron.*, vol. 35, no. 6, pp. 6533–6547, Jun. 2020.

[21] M. Bendjedia, Y. Ait-Amirat, B. Walther, and A. Berthon, "Position control of a sensorless stepper motor," *IEEE Trans. Power Electron.*, vol. 27, no. 2, pp. 578–587, Feb. 2012.

[22] L. Fang et al., "Design of wireless individual-drive system for variable-reluctance stepping motor," *IEEE Trans. Circuits Syst. II, Exp. Briefs*, vol. 69, no. 4, pp. 2141–2145, Apr. 2022.

[23] S. Li, W. Li, J. Deng, T. D. Nguyen, and C. C. Mi, "A double-sided LCC compensation network and its tuning method for wireless power transfer," *IEEE Trans. Veh. Technol.*, vol. 64, no. 6, pp. 2261–2273, Jun. 2015.

[24] Z. Pantic, K. Lee, and S. M. Lukic, "Multifrequency inductive power transfer," *IEEE Trans. Power Electron.*, vol. 29, no. 11, pp. 5995–6005, Nov. 2014.
[25] Z. Zhang, X. Li, H. Pang, H. Komurcugil, Z. Liang, and R. Kennel, "Multiple-frequency resonating compensation for multichannel transmission of wireless power transfer," *IEEE Trans. Power Electron.*, vol. 36, no. 5, pp. 5169–5180, May 2021.
[26] K. Song, Z. Li, J. Jiang, and C. Zhu, "Constant current/voltage charging operation for series–series and series–parallel compensated wireless power transfer systems employing primary-side controller," *IEEE Trans. Power Electron.*, vol. 33, no. 9, pp. 8065–8080, Sep. 2018.
[27] P. P. Acarnley, *Stepping Motors: A Guide to Theory and Practice*. London, U.K.: Institution Engineering Technology, 2002.

Songtao Li (Graduate Student Member, IEEE) received the B.Eng. and M.Eng. degrees in instrument science and technology from Southeast University, Nanjing, China, in 2018 and 2021, respectively. He is currently working toward the Ph.D. degree in electrical and electronic engineering with the University of Hong Kong, Hong Kong.

His current research interests include power electronics, wireless power transfer, and electric vehicle technologies.

K. T. Chau (Fellow, IEEE) received the B.Sc.(Eng.), M.Phil., and Ph.D. degrees in electrical and electronic engineering from The University of Hong Kong, Hong Kong, in 1988, 1991, and 1993, respectively.

He is currently a Chair Professor of electrical energy engineering with the Research Centre for Electric Vehicles and the Department of Electrical and Electronic Engineering, The Hong Kong Polytechnic University, Hong Kong. His research interests include electric and hybrid vehicles, power electronics and drives, and renewable energies. He is the author of nine books and more than 350 journal papers.

Dr. Chau is a Fellow of the Institution of Engineering and Technology, U.K., and the Hong Kong Institution of Engineers. He is also a Co-Editor for the *Journal of Asian Electric Vehicles*. He is a Chartered Engineer. He was the recipient of the Changjiang Chair Professorship from the Ministry of Education, China, and the Environmental Excellence in Transportation Award for Education, Training, and Public Awareness from the Society of Automotive Engineers International.

Wei Liu (Member, IEEE) received the B.Eng. and M.Eng. degrees in electrical engineering from the China University of Petroleum, Qingdao, China, and the Ph.D. degree in electrical and electronic engineering from The University of Hong Kong (HKU), Hong Kong, China, in 2014, 2017, and 2021, respectively.

He is currently an Assistant Professor with the Research Centre for Electric Vehicles and the Department of Electrical and Electronic Engineering, The Hong Kong Polytechnic University (PolyU), Hong Kong. He served as a Postdoctoral Fellow and a Research Assistant Professor from 2021 to 2023. He is currently an Honorary Assistant Professor with the Department of Electrical and Electronic Engineering, HKU. He also worked as a Visiting Researcher with Nanyang Technological University, Singapore, in 2019. His research interests include wireless power transfer, power electronics, biomedical power electronics, and electric vehicle technologies.

Dr. Liu was the recipient of the Power Engineering Prize from HKU, the Excellent Paper Award, and the Best Presentation Award from International Conferences in the area of Electric Vehicles and Transportation Electrification. He is also a Guest Associate Editor for the *IEEE Journal of Emerging and Selected Topics in Power Electronics (JESTPE)* and international journals, and the Session Chair of international conferences.

Chunhua Liu (Senior Member, IEEE) received the B.Eng. and M.Eng. degrees in automatic control from the Beijing Institute of Technology, Beijing, China, and the Ph.D. degree in electrical and electronic engineering from The University of Hong Kong, Hong Kong, in 2002, 2005, and 2009, respectively.

Since 2015, he has been with the City University of Hong Kong, Hong Kong, where he is currently a Professor of electrical and electronic engineering with the School of Energy and Environment. His research interests include electric machines and drives, electric vehicles and aircraft, electric robotics and ships, renewables and microgrids, power electronics, and wireless power transfer. In these areas, he has authored or coauthored more than 300 refereed papers. In addition, he is an RGC Research Fellow, a Distinguished Lecturer of IEEE Vehicular Technology Society, and World's Top 2% Scientists according to metrics compiled by Stanford University.

Dr. Liu is currently an Associate Editor for IEEE TRANSACTIONS ON INDUSTRIAL ELECTRONICS, and an Editor for IEEE TRANSACTIONS ON VEHICULAR TECHNOLOGY, IEEE TRANSACTIONS ON ENERGY CONVERSION, and *IEEE Power Engineering Letters*. Also, he is an Editor for *Energies*, Subject Editor for *IET – Renewable Power Generation*, an Associate Editor for the *Open Journal of the Industrial Electronics Society*, *IEEE Access*, *IEEE Chinese Journal of Electrical Engineering*, *CES Transactions on Electrical Machines and Systems*, and *Elsevier Green Energy and Intelligent Transportation*, and an Editor for IEEE TRANSACTIONS ON MAGNETICS – CONFERENCE, respectively. In addition, he is the Chair and Founder of both Hong Kong Chapter, IEEE Vehicular Technology Society, and Hong Kong and Guangzhou Joint Chapter, IEEE Industrial Electronics Society, respectively.

Chi-Kwan Lee (Senior Member, IEEE) received the B.Eng. and Ph.D. degrees in electronic engineering from the City University of Hong Kong, Hong Kong, in 1999 and 2004, respectively.

He was a Lecturer with the Hong Kong Polytechnic University from 2008 to 2012. In 2012, he joined the University of Hong Kong, where he became an Associate Professor in 2018. From 2010 to 2020, he was a Visiting Researcher with Imperial College London, U.K. Since 2024, he has been holding the Professorship with the University of Technology Sydney, Australia. His research interests include electric power conversion, electromagnetic devices, wireless power transfer, renewable energy, and smart grid technologies.

Dr. Lee was a recipient of the 2015 IEEE POWER ELECTRONICS SOCIETY TRANSACTIONS First Prize Paper Award for his publications on Wireless Power Transfer. He serves on the steering committee and was the General Chair of the 2018 IEEE PELS Workshop on Emerging Technologies: Wireless Power. He is an Associate Editor for the IEEE TRANSACTIONS ON POWER ELECTRONICS and *IEEE Journal of Emerging and Selected Topics in Power Electronics*.